Influence of a magnetic field on an extreme ultraviolet photon-induced plasma afterglow

Please check the document version of this publication:

• A submitted manuscript is the version of the article upon submission and before peer-review. There can be important differences between the submitted version and the official published version of record. People interested in the research are advised to contact the author for the final version of the publication, or visit the DOI to the publisher's website.
• The final author version and the galley proof are versions of the publication after peer review.
• The final published version features the final layout of the paper including the volume, issue and page numbers.

[Link to publication](#)

Influence of a magnetic field on an extreme ultraviolet photon-induced plasma afterglow

IOP ebooks™

Bringing together innovative digital publishing with leading authors from the global scientific community.

Start exploring the collection−download the first chapter of every title for free.

Influence of a magnetic field on an extreme ultraviolet photon-induced plasma afterglow

R Limpens[1,2] , B Platier[1,2,*] , A C Lassise[2], T J A Staps[1] , M A W van Ninhuijs[1] ,
O J Luiten[1] and J Beckers[1,*]

[1] Department of Applied Physics, Eindhoven University of Technology, PO Box 513,
5600MB Eindhoven, The Netherlands
[2] ASML Netherlands B.V., De Run 6501 5504DR Veldhoven, The Netherlands

E-mail: b.platier@tue.nl and j.beckers@tue.nl

CrossMark

Abstract
Understanding extreme ultraviolet (EUV) photon-induced plasma dynamics is key to increasing
the lifetime of the new generation of lithography machines. The plasma decay times were
determined by means of a non-destructive microwave method, microwave cavity resonance
spectroscopy, for unmagnetized and magnetized EUV photon-induced plasma afterglows with
the argon pressure ranging from 0.002 to 10 Pa. As a result of an external magnet with a
magnetic field strength of (57 ± 1) mT, the plasma decay times were extended by two orders of
magnitude. Good agreement was found between these measured plasma decay times and four
diffusion models, i.e. the ion acoustic, ambipolar, classical-collision, and Bohm's diffusion
model.

Keywords: EUV photon-induced plasma, afterglow, magnetic field, microwave cavity, MCRS,
magnetized, plasma

(Some figures may appear in colour only in the online journal)

1. Introduction

The world today becomes increasingly dominated by electronic devices, all operating using integrated circuits embedded into microchips. In order to create microchips with smaller circuits, photolithography can apply light with a shorter wavelength. The fabrication of the newest generation chips utilizes extreme ultraviolet (EUV) photons, which have a wavelength of only 13.5 nm [1]. In this fabrication process, a low-pressure background gas (typically 1–10 Pa of H_2 [2]) is intentionally injected in the lithography machine to increase the lifetime of the valuable optical components by, e.g. removal of carbon [3–6]. When the pulsed beam of 92 eV photons travels through the gas, it partially ionizes the gas, resulting in the creation of a highly-transient weakly-ionized plasma [7]. After the irradiation period, the so-called EUV-induced plasma decays, where the plasma during the decay process is generally referred to as the plasma afterglow. The fundamental investigation of EUV-induced plasma afterglows and their governing processes is key for further development of the new generation of lithography machines.

An EUV-induced plasma afterglow has a number of unique properties, which are a result of its typical formation process and its highly transient dynamics. For instance, the initial electron energy distribution function (EEDF) is atypical, because the bulk of the electrons in the plasma is created through photo-ionization [8]. Subsequently, these highly energetic electrons with an average energy of 66 eV [8] can further ionize the gas through electron impact ionization,

---

* Authors to whom any correspondence should be addressed.

creating additional electrons [9]. As a result of this process, the maximum plasma density is reached within 500 ns and the initial EEDF greatly deviates from a Maxwellian distribution [9, 10]. After the creation process, the electrons thermalise to room temperature (due to collisions with the background gas) and the plasma decays, with its decay rate depending on the background gas pressure. Since the ionization degree of the plasma is low [9], little volume recombination occurs, such that the main loss channel of the charged particles is recombination at the wall [8]. Therefore, the plasma diffusion mechanisms are closely related to the decay of the plasma. These properties make an EUV-induced plasma an interesting system to investigate the fundamental plasma diffusion processes.

In this study, a non-destructive method, microwave cavity resonance spectroscopy (MCRS), is applied to investigate the diffusion processes in these EUV-induced plasma afterglows by measuring the evolution of the electron density. The diffusive mechanisms governing the plasma decay depend, among others, on the electron mean free path and the initial plasma dimensions [9]. Recently, the sensitivity of MCRS has been increased [11–15], enabling the exploration of a third decay regime [11]. This provided in-depth insight into the low-density electron dynamics of an EUV-induced argon plasma, late in the afterglow.

The newest development [16] in this field utilizes a static magnetic field to confine an EUV-induced plasma to extend its lifetime and thus increase the operational range [17] of the MCRS technique. Besides the improvement of the MCRS method, studying the governing diffusion processes is intriguing from a fundamental point of view, since not all diffusion models remain valid in the applied gas pressure range [18–23]. Although enabled by the aforementioned developments, the experimental conditions have not been described in literature. This paper, therefore, investigates the validity of various diffusion models in EUV-induced plasma afterglows for pressures ranging from 0.002–10 Pa and uses the addition of an axial magnetic field as an independent experimental 'knob' to study the relevant elementary processes.

2. Experimental configuration and methods

The experimental setup consisted of a data-acquisition system, which is described in section 2.2, and three vacuum chambers: the source, collector, and measurement chamber. All three vacuum chambers and their functionalities are discussed below. Figure 1 shows the measurement chamber with the relevant diagnostics and electronics.

In the source chamber, xenon gas was ionized by applying a high voltage between two electrodes in a hollow cathode configuration. Due to Lorentz forces, caused by the high discharge currents, the plasma is pinched to a narrow channel with a high resistance. The Ohmic heating of the discharge leads to highly ionized xenon, which emits EUV photons. By applying short voltage pulses on the electrodes in a repetitive manner, EUV light with a pulse duration of 100 ns and a repetition rate of 497 Hz was produced. Despite that the typical repetition rates of sources in lithography tools is much higher, this study is still highly valuable for creating a better understanding of the fundamental processes in this type of plasma. Moreover, the decay of the plasma, which is the focus of this paper, is to this extent not influenced by the repetition rate [9]. A spectral purity filter (SPF) was used to mimic EUV lithography relevant conditions, i.e. by rejecting photons with wavelengths longer than 20 nm. This EUV source and the used SPF are further discussed in, for example, [9]. The in-band (12–20 nm) pulse energy ranged from (8 ± 2) to (12 ± 2) μJ, which was reduced on purpose compared to prior work [8, 24–27] to decrease the maximum electron density. This was done to ensure that the induced plasma decayed before the next EUV pulse was initiated.

In the collector chamber, the EUV light was focused using a layered nested set of mirrors, a so-called Wolter mirror, to the focal point, located in the measurement chamber (see figure 1). A hollow metal cone with at its narrow-end an opening of 2 mm in diameter was used to prevent the creation of photo-electrons by EUV radiation in the measurement volume, and to enable differential pumping between the collector and measurement chamber.

In the measurement chamber, the spectrally purified EUV beam reached the focal spot. This focal spot was located in the center of a hollow cylindrical metal structure: the resonance cavity, which was used to perform MCRS measurements. The principles of this diagnostic method are explained in the paragraph below. The cavity had a radius of $R = 33$ mm and a length of $L = 16$ mm. Its end-plates included two 13 mm diameter concentric holes to allow the EUV radiation to pass through the cavity without hitting the inner cavity walls. The cavity was aligned such that the EUV beam traversed the cavity along its symmetry axis. To introduce the microwaves in the resonance cavity, a linear antenna with a diameter of 1 mm and a length of ~ 1 cm protruded the volume.

The cavity was enclosed by a removable hollow cylindrical NdFeB (grade: GSN-52) magnet with an inner radius of 76 mm, an outer radius of 95 mm, and a length of 120 mm (see yellow structure in figure 1). COMSOL Multiphysics® software was used to compute the average magnetic field magnitude B and the magnetic field profile. These simulations indicated that $B = 61$ mT and that, as a result of the geometry of the magnet, the field is uniform at the position of the cavity. The magnitude of the magnetic field was also measured by a Hall effect sensor at the position of the cavity and resulted in $B = (57 \pm 1)$ mT, which agrees reasonably well with the values of the simulated field. These measurements also confirmed that the magnetic field magnitude at the position of the cavity is uniform, taking into account the measurement accuracy. These simulations and measurements were also used in [16]. In the cavity, the magnetic field pointed towards the EUV source as is indicated by the direction of 'B' in figure 1.

Despite that a study with H_2 as a background gas in the measurement chamber would be extremely useful, in this investigation argon is used for the reason that the magnet
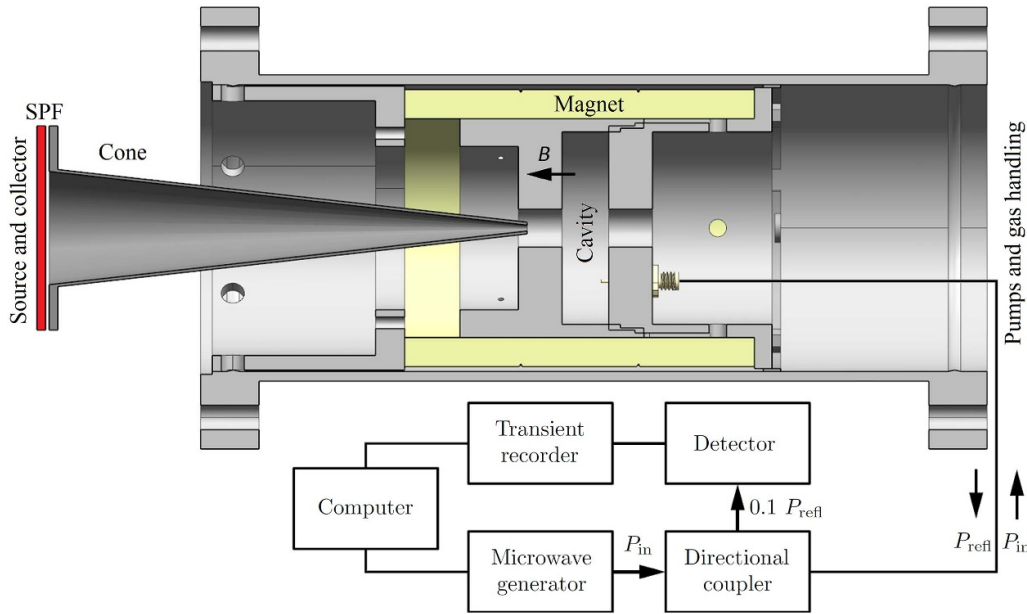
Figure 1. Schematic overview of the experimental setup. Reproduced from [15], with the permission of AIP Publishing.

material reacts with H_2. The difference in ion mass of argon and hydrogen results in longer plasma decay in argon due to the increased ion mobility [28]. However, the fundamental diffusion processes are similar.

To maintain an argon atmosphere in the resonant cavity and control the gas pressure in it, the measurement chamber was outfitted with a gas inlet, butterfly valve, turbo pump, and prepump. In the experiments discussed in this paper, the pressure was varied over the range of 0.002–10 Pa.

2.1. Microwave cavity resonance spectroscopy

Since the 1940s, the MCRS diagnostic technique relies on measuring changes in the resonant behavior of an electromagnetic standing wave and relating these changes to material properties, e.g. the electron density [29]. In experiments, an electromagnetic field is generated in a void in a metal structure, i.e. the cavity. When there is no plasma in the cavity, the resonance frequency of the field is referred to as f_0. Free electrons affect the permittivity of a material, which influences the electromagnetic fields in the cavity. This perturbation of the resonant field leads to a shift of the resonance frequency to f_{res} for a plasma-filled cavity.

The temporally resolved measurable shift $\Delta f(t) = f_{res}(t) - f_0$ corresponds to

$$\frac{\Delta f(t)}{f_0} = \frac{e^2}{8\,\pi^2\,m_e \varepsilon_0\,f_{res}^2(t)}\,\overline{n}_e(t). \qquad (1)$$

Here, m_e denotes the electron rest mass, e the elementary charge, and ε_0 the vacuum permittivity. The value of $\overline{n}_e$, obtained from equation (1), is the electric-field-squared-weighted and cavity volume-averaged electron density:
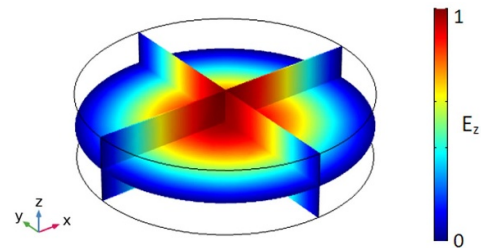
Figure 2. Normalized values of the *z*-component of the electric field of the applied resonant mode TM_{010}. This simulation was conducted in COMSOL Multiphysics® software.

$$\overline{n}_e \equiv \frac{\underset{\text{cavity}}{\int}\,n_e(\boldsymbol{x})|\boldsymbol{E}(\boldsymbol{x})|^2 d^3\,\boldsymbol{x}}{\underset{\text{cavity}}{\int}\,|\boldsymbol{E}(\boldsymbol{x})|^2 d^3\,\boldsymbol{x}}, \qquad (2)$$

where $\boldsymbol{E}(\boldsymbol{x})$ represents the local electric field profile of the active resonant mode at position $\boldsymbol{x}$, and similarly $n_e(\boldsymbol{x})$ the local electron density.

In the current work, the TM_{010} mode with a resonance frequency of $f_0 = 3.5$ GHz was excited. The TM_{010} mode is selected because of its large electric field amplitude in the *z*-direction, which is along the propagation direction of the EUV beam, at the center of the cavity (see figure 2). This means that the electron density is most sensitively probed at the center of the cavity, where the EUV beam travels through and, hence, where the initial plasma is created.

Generally, equation (1) becomes invalid when the plasma is subjected to a magnetic field due to the introduction of additional terms in the dielectric tensor. However, under the assumption that the electric field components of TM modes only point in the *z*-direction, the permanent magnetic field,

which also points in the *z*-direction, has no effect on the resonance frequency. This is the result of the properties of the dielectric tensor, which can be expressed as [30, 31]

$$\overline{\overline{\varepsilon}} = \begin{bmatrix} \varepsilon_{xx} & -i\varepsilon_{xy} & 0 \\ i\varepsilon_{xy} & \varepsilon_{yy} & 0 \\ 0 & 0 & \varepsilon_{zz} \end{bmatrix}, \tag{3}$$

where *i* denotes the imaginary unit. The definitions of the dielectric tensor components $\varepsilon_{xx} = \varepsilon_{yy}$, ε_{xy}, and ε_{zz} can be found in literature, see, for example [31]. A shift in the resonance frequency due to a change in the permittivity is based upon the operation $\overline{\overline{\varepsilon}}\mathbf{E}$. Since—for the applied TM mode—the $\mathbf{E} = E_z\hat{z}$, with $\hat{z}$ the unit vector in the z-direction, only the ε_{zz} of the dielectric tensor in equation (3) remains. This parallel component (with respect to the external magnetic field **B**) represents the plasma permittivity, $\varepsilon_{zz} = \varepsilon_{r,\text{plasma}} \approx 1 - f_{\text{pe}}^2/f_0^2$, where f_{pe} represents the plasma electron frequency [31]. This approximation is valid because the electron-neutral collision frequency is negligible with respect to f_0 for the relatively low gas pressures in the presented work.

2.2. Data acquisition system

A schematic of the data acquisition system is presented in figure 1. The system was similar to the ones used in prior studies [11, 16, 32]. The data acquisition system consisted of the following: a Stanford Research Systems SG386 microwave generator produced a sinusoidal signal with a frequency, *f*, and power, P_{in}. These waves traveled through a Mini-Circuits ZHDC-16-63-S+ directional coupler, which separated forward and reverse traveling signals. After this coupler, the microwaves were applied to the antenna. Depending on the applied value of *f*, a certain part of the input power was reflected, denoted by P_{refl}. At resonance, P_{refl} is minimal and the applied frequency is then called the resonance frequency. The reflected power signal was returned to the directional coupler and was measured by a Hittite 602LP4E logarithmic detector. The output of the logarithmic detector was then sampled at 25 MHz by a Spectrum M3i.4121-exp transient recorder and saved by a computer for post-measurement analysis. Since the EUV pulses were highly-reproducible, 128 reflected power measurements were averaged to improve the signal-to-noise ratio. A spectral range of 55 MHz, with a step size of 20 kHz, was scanned and its response saved using an in-house developed computer program. The resonance frequency was obtained post-measurement by fitting the reflected microwave power signal, P_{refl}, and determining the minimum of this fit. The same approach with a moving average filter (temporal width = 1 μs) as used in [11, 14] was employed here to increase the spectral resolution to 2×10^2 Hz.

3. Results: electron density decay experiments

The electron density evolution of an EUV-induced plasma afterglow in argon is determined using MCRS both without and with a static magnetic field for background pressures ranging from 0.002 to 10 Pa. For 10 Pa, the magnetic field extends
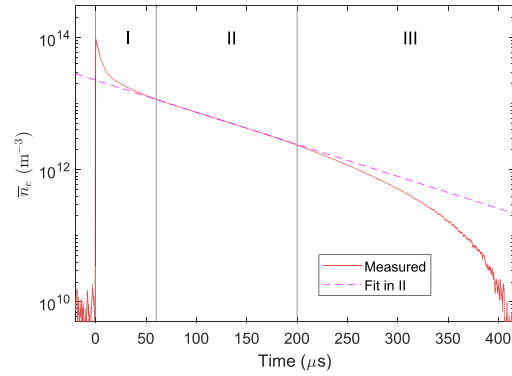

Figure 3. Electric-field-squared-weighted volumed-averaged electron density, $\overline{n}_e$, as a function of time, *t*, for an argon plasma induced by EUV radiation with a pulse energy of (9 ± 2) μJ and without the presence of the external magnetic field. A SPF was used and an argon background pressure of 5 Pa was applied. The three distinct decay phases are indicated by Roman numerals (I–III). A moving average filter of 1 μs was used in phases II and III to reduce noise. Reproduced from [15], with the permission of AIP Publishing.

the lifetime of the plasma beyond the pulse period, resulting in invalid data for the differential measurement scheme. For this reason, the magnetized plasma data for pressures higher than 5 Pa are not presented. After the plasma is created by photo-ionization and electron impact ionization, the electron density decays. Depending upon the initial plasma conditions, this decay process can be separated in two or three distinct phases [11].

In section 3.1, these three decay phases are discussed for a typical unmagnetized EUV-induced plasma afterglow. In section 3.2, the remaining experiments are presented, both without and with the presence of the magnet. The unmagnetized experimental results are in agreement with previous studies [8, 9, 27]. The results of a magnetized EUV-induced plasma afterglow are for the first time presented for gas pressures between 0.002 and 1 Pa. In order to quantitatively compare these results to each other and to theory, the 1/*e* plasma decay time during phase II is determined for each experimental configuration.

3.1. A typical electron density evolution during the plasma decay

Figure 3 shows a typical evolution of $\overline{n}_e$ during the decay of a 5 Pa argon EUV-induced plasma afterglow without the presence of the magnet. At $t = 0$, the plasma is created by the short EUV pulse, which subsequently decays following three distinct, consecutive phases. Each of these decay phases will only be briefly described below, since the authors refer to [9, 11, 27] for more in-depth descriptions of these phases.

In *phase I*, the $\overline{n}_e$ decays rapidly. This rapid decay is the result of the plasma expansion towards the walls and the loss of the fast electrons at the wall. In this process, less electrons are probed by the active resonant mode (figure 2). In addition, these electrons are probed in regions with a smaller electric field strength. Since the MCRS technique is most sensitive
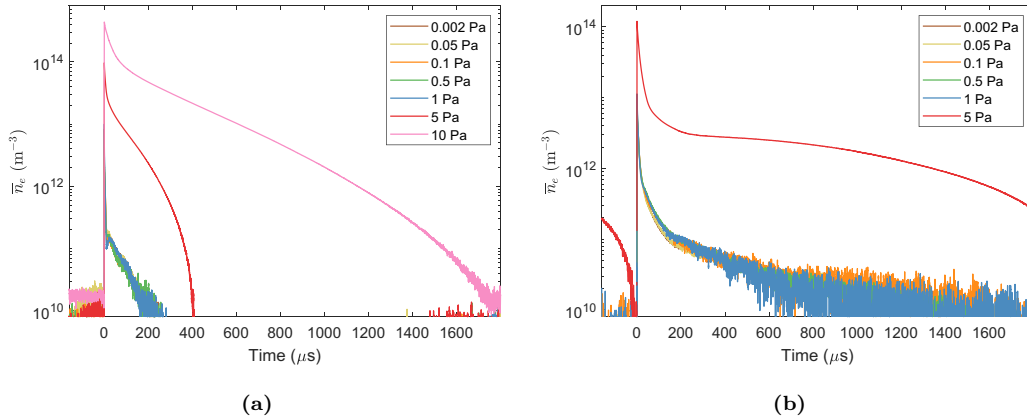
Figure 4. The electric-field-squared-weighted volume-averaged electron densities, $\overline{n}_e$, as a function of time for various background pressures (a) without and (b) with the presence of the magnet with a magnitude of (57 ± 1) mT. At $t = 0$, the argon plasma is created by EUV radiation with a pulse energy ranging from (8 ± 2) to (12 ± 2) μJ. A moving average filter of 1 μs (25 data points) is applied to smoothen the data, with the exception around $t = 0$ to maintain the correct values for the maximum detected $\overline{n}_e$.

at the maximum magnitude of the electric field of the resonant mode, this selective sensitivity results in an evident rapid decay. This process continues until the plasma has fully expanded and the remaining plasma electrons are confined by the self-induced electric field from the plasma.

In *phase II*, the $\overline{n}_e$ decays exponentially, which is driven by ambipolar transport towards the walls. Subsequently, the electrons are lost at the wall due to recombination [8] or they escape to ground (as the cavity was grounded). In this region, an exponential fit can be used to determine the $1/e$ plasma afterglow decay time, τ, of this phase. The determination of τ depends on the start and end-time of phase II (60 and 200 μs, respectively, in figure 3) and is insensitive to relatively small differences in these values. The plasma afterglow decay time will later in this paper be used to quantitatively compare the explored (un)magnetized plasma afterglows.

In *phase III*, the electron density decay rate accelerates. Due to the low electron density, the Debye length has become sufficiently large—compared to the cavity geometry—such that the plasma decay is governed by free diffusion instead of ambipolar diffusion. This regime has recently been studied for the first time [11].

3.2. Plasma afterglow decay times

The evolution of the electric-field-squared-weighted volumed-averaged electron density is determined for pressures ranging from 0.002 to 10 Pa without and with the presence of the magnetic field (figures 4(a) and (b), respectively). Preliminary analysis of these two graphs clearly shows that the magnetic field greatly reduces the electron density decay rate, resulting in an increase of the plasma lifetime. Furthermore, figure 4 shows that the 0.002–1 Pa decay experiments practically overlap, while the $\geqslant 5$ Pa experiments are detached. These distinct types of electron density decay rates are expected from a theoretical point of view and have been repeatedly discussed in literature [9, 20–22, 33] for similar plasma afterglow experiments.

For the experiments without magnetic field, negative shifts up to 6×10^2 Hz have been measured resulting in negative apparent electron densities. Due to logarithmic plotting in figure 4(a), these apparent negative $\overline{n}_e$ are not visible. Although these negative shifts have been investigated in prior works [9, 16], a conclusive explanation of negative shifts of such an extent is absent. Since the effect is beyond the scope of the current study, which focuses on the decay in the higher $\overline{n}_e$ regimes. Note that these apparent negative shifts are ~ 3 orders of magnitude smaller than the maximum shift induced by the plasma.

Taking into account the highly transient nature of the decay process, no complete theory exists that describes this decay fully. Therefore, only the decay during phase II, which is best understood but still largely unexplored, is compared to models to enhance understanding. By means of an exponential fit in this phase (an example fit was shown in figure 3), the plasma afterglow decay time is determined for each case (without and with the presence of the magnetic field and for each set value of the applied gas pressure), as illustrated in figure 5. The decay times, obtained through measurements of the $\overline{n}_e$, are indicated by points, while the dotted lines indicate the theoretical decay times based on four different diffusion models, which will be discussed in the next section. As observed in figure 4, the magnetic field reduces the plasma afterglow decay rate: the decay times clearly show an increase over the applied pressure range. Furthermore, for both experiments without and with the presence of the magnet, two distinct decay trends are observed as a function of the gas pressure. In order to explain these trends, the underlying physical mechanisms and models are required, which will be presented in the next section.

4. Discussions and interpretations

In the current experiments, multiple factors influence the plasma decay process, such as cavity geometry, gas pressure, and magnetic field strength. The geometry of the cavity
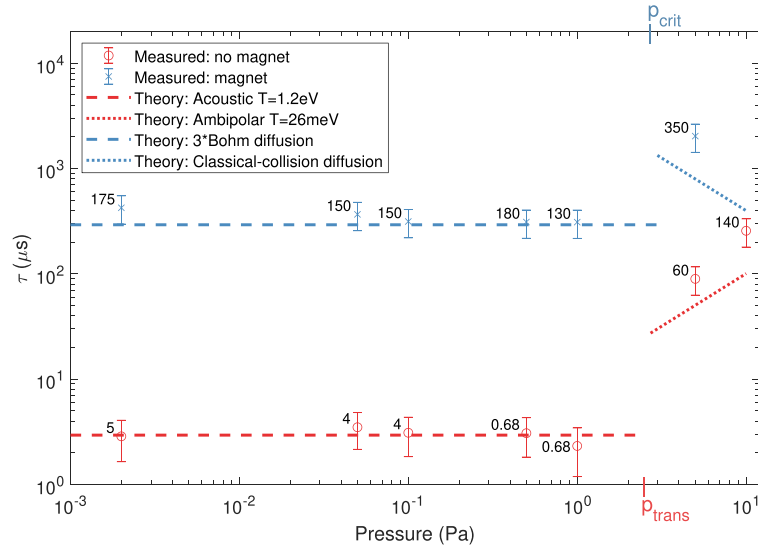
Figure 5. The EUV photon-induced argon plasma afterglow decay times with a SPF for various applied gas pressures. These $1/e$ decay times are obtained during phase II by means of an exponential fit in the electric-field-squared-weighted volume-averaged electron density graphs for each pressure. The numbers close to the measured decay times indicate the time (in μs) at which the fitting procedure started. This time is also directly related to the temperature of the electrons, since these rapidly cool down.

strongly influences the diffusion of plasma species towards the wall, as a result of the imposed boundary condition that states that the density must be approximately zero at these walls. In the case of a finite cylinder with radius, R, and length, L, the following diffusion length, Λ, is used [34]

$$\Lambda = \left[\left(\frac{x_{01}}{R} \right)^2 + \left(\frac{\pi}{L} \right)^2 \right]^{-1/2}. \quad (4)$$

Here, the factor $x_{01} = 2.405$ results from the first root of the equation $J_0(x) = 0$, where J_0 represents the zeroth order Bessel function of the first kind. For the used cavity dimensions, the diffusion length is $\Lambda = 4.8 \pm 0.2$ mm. However, as a result of the 13 mm holes in the cavity end-plates, which allow the EUV beam to traverse, this value is an underestimate. Based upon simulations [9] performed for a similar geometry, the effective diffusion length is estimated to be $\Lambda \approx 5$ mm.

The analysis of the obtained decay times is based upon four different diffusion models as a result of the four different observed $\bar{n}_e$ decay trends. In the following section, the plasma afterglow experiments without magnetic field will be discussed and after that the experiments with magnetic trapping of the plasma will be treated. Both experimental conditions are divided as a function of the gas pressure into two regimes. The decay times obtained from the experiments and models are presented in figure 5 by the symbols and lines, respectively. In this figure, the color red is used to indicate the decay times of the unmagnetized plasma, while blue is used for the data with magnetic field present.

4.1. Unmagnetized plasma afterglow

The unmagnetized electron density decay rates were investigated extensively in a prior study [8] and the presented results here serve as validation and reference for the experiments with

magnet. Both in the case of our measurements (see figure 5), as well as in this prior work, two distinct trends in the decay rate as a function of gas pressure can be observed. An increase in background pressure results in more collisions and, consequently, in a decrease of the ion mean free path. Generally, ions are the slowest species in a plasma; therefore, the ions dominate most diffusion processes [31]. For unmagnetized EUV photon-induced plasma afterglows and depending on the gas pressure, the mean free path of the ions, λ_i, can become shorter or longer than the initial (at $t = 0$) plasma radius r_{plasma}.

The inequality $\lambda_i > r_{plasma}$ holds for argon pressures below 2.4 Pa and implies that the plasma expansion is governed by the ion acoustic speed [9] for low gas pressures. If the argon gas pressure exceeds 2.4 Pa, $\lambda_i < r_{plasma}$ holds, and the plasma afterglow evolution in decay phase II is governed by ambipolar diffusion [8]. Hence, between the governing mechanisms, a transition pressure, p_{trans} (i.e. around an argon pressure of $p_{trans} = 2.4$ Pa), exists for the unmagnetized plasma afterglow experiments. This theoretical transition pressure is in agreement with the measured decay times presented in this work (see figure 5).

4.1.1. Ion acoustic diffusion regime.
For $p < p_{trans}$, the plasma expansion (after the highly energetic electrons have escaped to the wall to form a potential well) is governed by the ion acoustic speed, $u_{acoustic} = \sqrt{eT_e/m_i}$, where T_e denotes the electron temperature in eV, and m_i the mass of the ions. As a result of the aforementioned equation and for a constant electron temperature, which typically is 1.2 eV in this phase of the decay [9], the τ is constant as well. The ion acoustic governed decay time, $\tau_{acoustic}$, is given by [9]

$$\tau_{acoustic} = \frac{\Lambda}{u_{acoustic}} = \Lambda \sqrt{\frac{m_i}{eT_e}}. \quad (5)$$

As can be seen in figure 5, the ion acoustic speed model, with an electron temperature of 1.2 eV, describes the measurements well. Because the fitting procedure started early in the plasma afterglow, between 0.68 and 5 μs, the electrons still carry most excess energy and must be considered non-Maxwellian. Assuming that a 'temperature' can be determined this early in the afterglow, therefore, is arguable. However, the value found for T_e agrees well with those from previous MCRS experiments [9], performed under similar conditions.

4.1.2. Ambipolar diffusion regime. For pressures exceeding the transition value, $p > p_{trans}$, additional collisions occur and ambipolar diffusion governs the electron density decay in phase II (see figure 3). The ambipolar diffusion decay time τ_{amb} is [16]

$$\tau_{amb} = \Lambda^2 \frac{m_e \nu_{eff,en} + m_i \nu_{in}}{e(T_e + T_i)}, \tag{6}$$

where $\nu_{eff,en}$ denotes the effective electron-neutral collision frequency, ν_{in} the ion-neutral collision frequency, and T_i the ion temperature in eV.

The effective electron collision frequency can be calculated by [32, 35, 36],

$$\nu_{eff,en} = \frac{\int_0^\infty \epsilon^{3/2} e^{-\epsilon/eT_e} \frac{\nu_{en}(\epsilon)}{\nu_{en}^2(\epsilon) + 4\,\pi^2 f_0^2} d\epsilon}{\int_0^\infty \epsilon^{3/2} e^{-\epsilon/eT_e} \frac{1}{\nu_{en}^2(\epsilon) + 4\,\pi^2 f_0^2} d\epsilon}, \tag{7}$$

where ν_{en} denotes the elastic electron-neutral collision frequency, which is a function of the electron energy ε. The range of probing frequencies was small compared to f_0 and, therefore, f_0 is assumed constant. Although initially the EEDF is highly non-Maxwellian, the fitting procedure started after most volume processes occurred, i.e. after phase I. The electrons rapidly lose their excess energy and are thermalised at the start of phase II [27]. Hence, the Maxwellian energy distribution function [37], $f(\epsilon) = 2\pi^{-1/2} T_e^{-3/2} e^{-\epsilon/eT_e}$, has been used to obtain equation (7).

The elastic electron-neutral collision frequency is derived from equation (3.1.8) in [31], while using the ideal gas law:

$$\nu_{en}(\epsilon) = \sigma_{en}(\epsilon) \frac{p}{eT_n} \sqrt{\frac{2\,\epsilon}{m_e}}, \tag{8}$$

where p is the gas pressure, T_n is the (neutral) gas temperature in eV, which is assumed to be equal to the room temperature, and $\sigma_{en}(\epsilon)$ is the electron-neutral cross-section, which depends on the energy of the electrons. The cross-section data for argon to calculate ν_{en} is obtained from the Phelps database [38].

The ion-neutral collision frequency is derived from equation (3.1.8) in [31], while using the ideal gas law and substituting the velocity with the thermal velocity:

$$\nu_{in} = \frac{\sigma_{in} p}{\sqrt{m_i e T_i}}, \tag{9}$$

where σ_{in} denotes the elastic ion-neutral cross-section which is 8×10^{-19} m^2 [31]. In the previous equation, the ion temperature, T_i, is assumed to equal room temperature ($T_i = T_n = 26$ meV).

The results obtained from the ambipolar model, equation (6), are indicated in figure 5 by the red dotted line. As can be seen, for an increasing gas pressure, more collisions occur, causing the plasma decay rate to be slower than at lower pressures. Due to the additional collisions and the higher initial electron density, the fitting procedure started after 60 and 140 μs. As a result, the plasma is in thermal equilibrium and the electrons have thermalised down to room temperature, i.e. 26 meV. Having room temperature electrons under these conditions agrees well with the electron temperatures found in similar studies [8–10].

As can be seen in figure 5, the obtained decay times are a factor ~ 2 higher than is expected from the ambipolar diffusion model. This means that the plasma decays slower than is anticipated by the model. We attribute these discrepancies to the limitations of the ambipolar diffusion model, which cannot include all the relevant physics. In view of the physics involved, the discrepancies are relatively small [16].

4.2. Magnetized plasma afterglow

The magnetic field clearly reduces the plasma afterglow decay rate (figures 4 and 5). Preliminary analysis of the magnetized plasma afterglow decay time (blue data points in figure 5) clearly shows two distinct trends separated by a critical pressure, p_{crit}. It is important to note that the underlying physical mechanisms for these two trends differ from the plasma afterglow experiments without magnet, which is associated with the initial plasma radius and argon pressure. In the case of the magnetized plasma decay times, the classical-collision and Bohm's diffusion model are in good agreement with the experimentally obtained values.

4.2.1. Classical-collision diffusion regime. The classical-collision diffusion model is similar to the ambipolar diffusion description with the difference that an extra term is introduced to include the magnetic field. From this model, we find the extended ambipolar diffusion decay time [16]:

$$\tau_{c-c} \approx \Lambda^2 \frac{m_e \omega_{ce}^2}{\nu_{eff,en} e(T_e + T_i)}, \tag{10}$$

where $\omega_{ce} = eB/m_e$ denotes the electron gyro-frequency. In this model, it is assumed that the cross field ion mobility is many times larger than the one of the electrons, $\mu_{\perp i} \gg \mu_{\perp e}$: the magnetic field is sufficiently strong to confine the electrons, while it is insufficient to confine the heavy argon ions in the same manner. Moreover, the electrons are assumed to be well-confined, $\omega_{ce} \gg \nu_{eff,en}$. Physically this assumption means that the magnetic field is dominant over the collisions between the electrons and neutrals; hence, the bulk of the electrons drift

along the magnetic field lines. Both these assumptions hold for the magnetized 5 Pa experiment, which agrees reasonably well with this model. The fitting procedure started at 350 μs; hence, the electrons are in thermal equilibrium at room temperature (26 meV) [9, 27]. This experiment shows, however, a slower diffusion rate than anticipated by equation (10).

Note that in both experiments (without and with the presence of the magnet) at 5 Pa the plasma decays slower than anticipated by the models. Although the plasma dynamics differ, a similar mechanism could be responsible for the slower decay rate predicted by the shared ambipolar diffusion coefficient. This mechanism could, for example, be related to the cavity geometry and the conductivity of its walls. Further experiments in the classical-collision diffusion regime are required to draw a more quantitative conclusion regarding the differences between the measurements and this model.

The classical-collision diffusion model has been extensively investigated in the past [39–43]. These studies showed that this model only holds under restricted conditions, i.e. below a so-called critical magnetic field strength B_{crit}. Equally significant but often not equally emphasized is the gas pressure, p_{crit}, which could also be considered critical to the confinement of the plasma afterglow. Observations show that, for argon pressures below 5 Pa, the obtained results deviate from the classical-collision diffusion model. Similar deviations have been reported repeatedly [18–21] for similar plasma afterglow experiments, where the charged particle transport transverse to the magnetic field was also higher than anticipated. This increased transport results in a shorter plasma afterglow decay time, which is in agreement with the obtained decay times in figure 5 for the 0.002–1 Pa experiments. This enhanced (anomalous) cross-field transport has so far been associated with instabilities of the plasma that generally occur at a critical magnetic field strength [44].

Theoretically determining the critical pressure for a magnetized plasma may be based upon the ratio between the elastic ion-neutral collision frequency ν_{in} and the ion cyclotron frequency $\omega_{\text{ci}} = eB/m_{\text{i}}$. This ratio $\omega_{\text{ci}}/\nu_{\text{in}}$ scales as the ratio between the magnetic field magnitude and the background gas pressure, B/p. If $\omega_{\text{ci}} > \nu_{\text{in}}$ then plasma instabilities may occur [44–46] that result in a different plasma evolution and, thus, alter the plasma afterglow decay time. For the magnet used in this work, the previous inequality holds for argon pressures below 2.6 Pa. This implies that a magnetized critical pressure exists of $p_{\text{crit}} = 2.6$ Pa (or a critical ratio of $p_{\text{crit}}/B_{\text{crit}} = 46$ Pa/T). This p_{crit} must not be confused with $p_{\text{trans}} = 2.4$ Pa for the unmagnetized experiments. This theoretical critical value is well in agreement with the observations in figure 5. Likely, the critical ratio ($p_{\text{crit}}/B_{\text{crit}}$) also depends on the geometry of the cavity, because the charged particles can short circuit [39] along the magnetic field lines (at the end-plates of the cavity) if the ions are well-confined.

4.2.2. Bohm diffusion regime.

Anomalous diffusion was observed for the magnetized plasma afterglows for gas pressures below $p_{\text{crit}} = 2.6$ Pa. Based upon a comprehensive

literature study [18, 20, 23, 44–50], a relation was found between this enhanced diffusion and the geometry of the cavity. As a result of the geometry, plasma oscillations could occur. Bohm *et al* [18] have proposed that plasma oscillations produce transverse electric fields along which charged particles may drift (transverse to the magnetic field). If this drift motion effect is dominant over the collisional transport, enhanced radial (transverse) diffusion occurs. This means that the diffusion coefficient is inversely proportional to the magnetic field strength. The plasma afterglow decay time then becomes [50],

$$\tau_{\text{Bohm}} = \frac{16\Lambda^2}{X}\frac{B}{T_e}, \qquad (11)$$

where X is a pre-factor which originally [18] equals 1.

For the observed experiments below $p_{\text{crit}} = 2.6$ Pa, the plasma afterglow decay times are approximately constant at $\tau = 300$ μs. The fitting procedure for this pressure regime started between 130–180 μs, which means that phase II started later compared to the experiments without magnet in this pressure regime. Hence, in the presence of the magnetic field, the plasma expansion towards the walls is delayed and the time at which volume processes take place is extended. The model of Bohm, including a pre-factor, shows the best agreement with the measured results, seen in figure 5. In order to correspond the measured decay times to this model, a pre-factor of $X = 3$ is required. This could either mean that the electron temperature is three times higher ($T_e = 3\,T_{\text{room}}$) or that this pre-factor contains an unknown enhanced diffusive phenomenon. According to literature [23, 44, 47–49], pre-factors, ranging from 1 to 10, are common for Bohm-type diffusion experiments and could be related to the geometry of the cavity.

The first indications of a transition towards much higher diffusion rates across a magnetic field have been studied in the past [20] and this transition mainly depends on the nature of the gas, its density, and the experimental geometry. Later [46], it was shown that plasma instabilities are closely related to both the length and radius of their cylindrical plasma chamber. Table 1 shows an overview of pre-factors that are available in literature for various ratios of L/R.

Experiments [44] where Langmuir probes have been used to measure the ion densities in pulsed electron beam induced helium plasma afterglows, showed Bohm-type diffusion with a pre-factor of $X = 0.4$ for $L/R = 15$. It is important to note that these probes are invasive, meaning that they interfere with the plasma. Other experiments [47], where the diffusion-driven currents towards the wall have been measured, also demonstrated that the plasma decay time depended on the ratio L/R. In the case that the plasma was enclosed by a metal cylinder with ratio $L/R = 8.75$, the diffusion appeared to be of Bohm-type with a pre-factor of $X = 2.2$ (for small values of p/B). In their work, similar experiments have been performed with a smaller radius, $L/R = 14$, while retaining the length of the enclosing metal cylinder. These measurements agree well with a pre-factor of $X = 1.75$. These results indicate that, for decreasing ratio L/R, the pre-factor for Bohm diffusion increases, as shown in table 1. Hence, based upon literature [44, 47], the

Table 1. Overview of Bohm pre-factors, *X*, for experiments where the plasma afterglow is enclosed by a metal cylindrical container with length, *L*, and radius, *R*.

Study	*L* (mm)	*R* (mm)	*L/R*	*X*
[44]	1500	100	15	0.4
[47]	700	50	14	1.75
[47]	700	80	8.75	2.2
Here	16	33	0.48	3

pre-factor of 3 found in this study could be justified by the small ratio of $L/R = 0.48$.

5. Conclusion

The electron dynamics in an EUV photon-induced plasma are investigated using a non-destructive microwave method, MCRS, for argon pressures ranging from 0.002 to 10 Pa. A magnetic field with a strength of (57 ± 1) mT has been employed to extend the lifetime of the plasma afterglow. Four diffusion models are applied to describe these (un)magnetized plasma afterglows.

For unmagnetized plasma afterglows, a transition pressure exists at 2.4 Pa, which is based upon the initial plasma (or EUV beam) radius and the ion mean free path. As a result, depending on the gas pressure, two different mechanisms govern the plasma decay for the case without the magnetic field: ion acoustic expansion and ambipolar diffusion.

Magnetized plasma afterglows also showed two distinct decay trends in which two different models are valid: classical-collision and Bohm's diffusion. Compared to the classical-collision diffusion model, enhanced diffusion is observed, which is common according to literature and is generally related to plasma instabilities. If these plasma instabilities are related to enhanced diffusion, these instabilities are likely caused by the magnitude of confinement (i.e. the ratio of p/B) and the cavity geometry.

This first detailed study of the decay of magnetized EUV photon-induced argon plasmas contributes to an improved understanding of the fundamental diffusion processes. Subsequently, this could help to improve the lifetime of the sensitive optical components in these tools.

Data availability statement

The data that support the findings of this study are available upon reasonable request from the authors.

Acknowledgments

ORCID iDs

R Limpens ⓘ https://orcid.org/0000-0002-5062-4554
B Platier ⓘ https://orcid.org/0000-0003-4524-0131
T J A Staps ⓘ https://orcid.org/0000-0002-9859-2942
M A W van Ninhuijs ⓘ https://orcid.org/0000-0002-0577-3403
J Beckers ⓘ https://orcid.org/0000-0001-6116-7013

References

[1] Feldman M 2013 *Nanolithography: The Art of Fabricating Nanoelectronic and Nanophotonic Devices and Systems* (Sawston: Woodhead Publishing)
[2] Beckers J, van de Ven T, van der Horst R, Astakhov D and Banine V 2019 *Appl. Sci.* **9** 2827
[3] Braginsky O *et al* 2012 *J. Appl. Phys.* **111** 093304
[4] Boller K, Haelbich R P, Hogrefe H, Jark W and Kunz C 1983 *Nucl. Instrum. Methods Phys. Res.* **208** 273–9
[5] Kuznetsov A, Gleeson M and Bijkerk F 2013 *J. Appl. Phys.* **114** 113507
[6] Van den Bos R, Lee C, Benschop J and Bijkerk F 2017 *J. Phys. D: Appl. Phys.* **50** 265302
[7] van der Velden M H L, Brok W J M, van der Mullen J J A M, Goedheer W J and Banine V 2006 *Phys. Rev. E* **73** 036406
[8] van der Horst R M, Beckers J, Osorio E A and Banine V Y 2015 *J. Phys. D: Appl. Phys.* **48** 285203
[9] van der Horst R M 2015 Electron dynamics in EUV-induced plasmas Ph.D. Thesis Eindhoven University of Technology
[10] Beckers J, van de Wetering F M J H, Platier B, van Ninhuijs M A W, Brussaard G J H, Banine V Y and Luiten O J 2018 *J. Phys. D: Appl. Phys.* **52** 034004
[11] Platier B, Limpens R, Lassise A C, Staps T J A, van Ninhuijs M A W, Daamen K A, Luiten O J, IJzerman W L and Beckers J 2020 *Appl. Phys. Lett.* **116** 103703
[12] van Ninhuijs M A W, Daamen K A, Franssen J G H, Conway J, Platier B, Beckers J and Luiten O J 2019 *Phys. Rev. A* **100** 061801
[13] Platier B, Staps T J A, van der Schans M, IJzerman W L and Beckers J 2019 *Appl. Phys. Lett.* **115** 254103
[14] Platier B, Staps T J A, Hak C C J M, Beckers J and IJzerman W L 2020 *Plasma Sources Sci. Technol.* **29** 045024
[15] Platier B, Staps T, Koelman P, van der Schans M, Beckers J and IJzerman W 2020 *Appl. Sci.* **10** 4331
[16] Platier B *et al* 2020 *Rev. Sci. Instrum.* **91** 063503
[17] Platier B, van de Wetering F M J H, van Ninhuijs M A W, Brussaard G J H, Banine V Y, Luiten O J and Beckers J 2020 *J. Phys. D: Appl. Phys.* **53** 359410
[18] Bohm D 1949 *Qualitative Description of the Arc Plasma in a Magnetic Field* (New York: McGraw-Hill)
[19] Bostick W H and Levine M A 1955 *Phys. Rev.* **97** 13–21
[20] Hoh F C and Lehnert B 1960 *Phys. Fluids* **3** 600–7
[21] Kadomtsev B B and Nedospasov A V 1960 *J. Nuclear Energy* C **1** 230–5
[22] Golant V E 1963 *Sov. Phys. Uspekhi* **6** 161–97
[23] Geissler K H 1968 *Phys. Rev.* **171** 179–80
[24] van der Horst R M, Jeckers J, Nijdam S and Kroesen G M W 2014 *J. Phys. D: Appl. Phys.* **47** 302001
[25] van der Horst R M, Osorio E A, Banine V Y and Beckers J 2015 *Plasma Sources Sci. Technol.* **25** 015012
[26] van der Horst R M, Beckers J, Osorio E A and Banine V Y 2015 *J. Phys. D: Appl. Phys.* **48** 432001
[27] Beckers J, van der Horst R M, Osorio E A, Kroesen G M W and Banine V Y 2016 *Plasma Sources Sci. Technol.* **25** 035010

J. Phys. D: Appl. Phys. **54** (2021) 435205

R Limpens *et al*

[28] van der Horst R M *et al* 2016 *J. Phys. D: Appl. Phys.*
     49 145203
[29] Biondi M A and Brown S C 1949 *Phys. Rev.* **75** 1700–5
[30] Gross S H and Felsen L B 1965 *J. Res.* **69D** 333–48
[31] Lieberman M A and Lichtenberg A J 2005 *Principles of
     Plasma Discharges and Materials Processing* 2nd ed
     (New York: Wiley)
[32] van der Schans M, Platier B, Koelman P, van de Wetering F M
     J H, van Dijk J, Beckers J, Nijdam S and IJzerman W 2019
     Plasma Sources Sci. Technol. **28** 035020
[33] Alikhanov S G, Zakharov V E and Khorasanov G L 1963
     Atomic Energy **14** 127–32
[34] Phelps A V 1990 *J. Res. Natl Inst. Stand. Technol.*
     95 407
[35] Whitmer R F and Herrmann G F 1966 *Phys. Fluids* **9** 768
[36] McColl W, Brooks C and Brake M L 1993 *J. Appl. Phys.*
     74 3724–35
[37] Lister G G, Li Y M and Godyak V A 1996 *J. Appl. Phys.*
     79 8993–7

[38] Phelps database (available at: www.lxcat.net) (Accessed 3
     May 2020)
[39] Simon A 1955 *Phys. Rev.* **98** 317
[40] Longmire C L and Rosenbluth M N 1956 *Phys. Rev.*
     103 507–10
[41] Bickerton R J and von Engel A 1956 *Proc. Phys. Soc.* B
     69 468–81
[42] D'Angelo N and Rynn N 1961 *Phys. Fluids* **4** 275
[43] D'Angelo N 1964 *Phys. Fluids* **7** 1086
[44] Dodo T 1969 *Plasma Phys.* **11** 881–7
[45] Pigache D R and Harding G N 1969 *Plasma Phys.* **11** 805–9
[46] Ventrice C A and Brown C E 1972 *J. Appl. Phys.*
     43 368–72
[47] Geissler K H 1968 *Plasma Phys.* **10** 127–36
[48] Pinheiro M J 2007 *J. Phys.: Conf. Ser.* **71** 012002
[49] Brenning N, Merlino R L, Lundin D, Raadu M A and
     Helmersson U 2009 *Phys. Rev. Lett.* **103** 225003
[50] Treumann R A, LaBelle J and Pottelette R 1992 Plasma
     transport through magnetic boundaries *Tech. rep.*